Heliyon 9 (2023) e14682

Contents lists available at ScienceDirect

Heliyon

journal homepage: www.cell.com/heliyon

Research article

3D printed superparamagnetic stimuli-responsive starfish-shaped hydrogels

Ali A. Mohammed [a,1], Jingqi Miao [b,1], Ieva Ragaisyte [b], Alexandra E. Porter [b], Connor W. Myant [a], Alessandra Pinna [b,c,*]

[a] Dyson School of Design Engineering, Imperial College London, SW7 2AZ, London, UK
[b] Department of Materials, Imperial College London, SW7 2AZ, London, UK
[c] The Francis Crick Institute, NW11 AT, London, UK

ARTICLE INFO

Keywords:
Super paramagnetic iron oxide nanoparticles (SPIONs)
3D printing
Additive manufacturing
Hydrogels
Magnetic stimuli
VAT photopolymerization

ABSTRACT

Magnetic-stimuli responsive hydrogels are quickly becoming a promising class of materials across numerous fields, including biomedical devices, soft robotic actuators, and wearable electronics. Hydrogels are commonly fabricated by conventional methods that limit the potential for complex architectures normally required for rapidly changing custom configurations. Rapid prototyping using 3D printing provides a solution for this. Previous work has shown successful extrusion 3D printing of magnetic hydrogels; however, extrusion-based printing is limited by nozzle resolution and ink viscosity. VAT photopolymerization offers a higher control over resolution and build-architecture. Liquid photo-resins with magnetic nanocomposites normally suffer from nanoparticle agglomeration due to local magnetic fields. In this work, we develop an optimised method for homogenously infusing up to 2 wt % superparamagnetic iron oxide nanoparticles (SPIONs) with a 10 nm diameter into a photo-resin composed of water, acrylamide and PEGDA, with improved nanoparticle homogeneity and reduced agglomeration during printing. The 3D printed starfish hydrogels exhibited high mechanical stability and robust mechanical properties with a maximum Youngs modulus of 1.8 MPa and limited shape deformation of 10% when swollen. Each individual arm of the starfish could be magnetically actuated when a remote magnetic field is applied. The starfish could grab onto a magnet with all arms when a central magnetic field was applied. Ultimately, these hydrogels retained their shape post-printing and returned to their original formation once the magnetic field had been removed. These hydrogels can be used across a wide range of applications, including soft robotics and magnetically stimulated actuators.

1. Introduction

Hydrogels possess unique mechanical, chemical and biological properties that have found applications across various research fields, such as soft actuators [1], bioelectronics and electronic skin [2,3], magnetic hydrogels for hyperthermia [4], amongst others. Hydrogels are hydrophilic materials composed of 3D polymeric networks capable of holding large amounts of water without breaking

* Corresponding author. Department of Materials, Imperial College London, SW7 2AZ, London, UK.
E-mail address: a.pinna@imperial.ac.uk (A. Pinna).
[1] Share first authorship.

https://doi.org/10.1016/j.heliyon.2023.e14682
Received 19 February 2023; Received in revised form 8 March 2023; Accepted 15 March 2023
Available online 28 March 2023

or rupturing. A wide range of polymers can be used to create hydrogels, allowing for custom functionalisation of the materials properties, such as the ability to respond to stimuli such as pH, temperature, light, electrical or magnetic fields [5]. However, their potential has largely been limited due to both their brittle nature and conventional fabrication techniques that limit the generation of prototypes with complex geometries for specific applications.

With recent advancements in technology and applied chemistry, hydrogels have become a popular material for additive manufacturing (AM) [6]. Zheng et al. used an extrusion-based printers to print an actuator composed of two layers of different tough physical hydrogels using multiple nozzles [7]. The programmed response of a dual-layered hydrogel in a solution with different ion concentrations provided the driving force for movement, offering a creative way of controlling soft robotic actuators. Similarly, Podstawczyk et al. prepared a 3D printing bio-nanocomposite ink composed of alginate, methylcellulose and magnetic nanoparticles (MNPs) for extrusion printing of remotely actuated hydrogels via a magnetic field [8]. Hydrogels play an important role in biomedical applications [9], drug delivery [10], tissue engineering [11–13], and wearable devices [14,15] for their ability to hold high water content [16], tuneable biodegradability [17–20], and biocompatibility [21]. These properties have resulted in a shift in attention towards hydrogels as a popular material for AM. Hydrogel networks are made of long hydrophilic polymer chains that are either physically, ionically or covalently crosslinked [21]. Among various polymerisation methods, photopolymerization provides more flexibility and ease for controlling the final 3D-printed product properties, reaching high pattern resolution and structural complexity with a fast-printing process [22,23]. Two commonly used photopolymerization-based 3D printing technologies are VAT photo-polymerization, also known as stereolithography (SLA) and digital light processing (DLP). They use the same principle but control the light sources in different ways. In SLA, a focused laser beam moves and scans the photo-resin point-by-point to initiate photo-polymerization, a vector scanning-based process. With DLP, a digital micromirror device is used to project a light mask and cure a whole layer of photo-resin all at once in several seconds (mask projection-based process) [24], accomplishing printing at a faster speed. When compared with SLA, DLP is faster but produces a less fine pattern-resolution. In SLA, resolution is based on a gaussian, laser point, with a fixed resolution that remains constant regardless of increased image size. With rapid development, the resolution of many commercial SLA printers in x, y, and z-axes can reach 20 μm for a cubic object [25], making them suitable for medical device manufacturing [26].

Due to the rapid advancement of nano scale engineering, various types of nanoparticles have been combined with different traditional materials for a range of applications. A previous study added cellulose nanocrystals (CNC) into a photo-resin for 3D printing in SLA, leading to an enhancement in mechanical properties with structural complexity [27]. Another example are 3D printed lattice cells by Wang et al. which exhibited negative thermal expansion, composed of PEGDA beams reinforced by copper nanoparticles [28]. Also, silica nanoparticles were used as fillers after surface modification to create electrolyte printable Li-ion batteries without decreasing the ionic conductivity [29]. The advantages of improved mechanical strength, flexibility and conductivity are also met with limitations during 3D printing. Some of these limitations include nanoparticle aggregation due to surface charges [30], sedimentation due to size or photo-resin viscosity [31], and reduced print accuracy due to light-scattering induced by nanoparticles [32,33]. Across the various types of nanoparticles, magnetic nanoparticles have a significant range of applications due to their magnetic properties, including many metals (Fe, Ni, Gd, Zn, Co, Mg) and their oxides, alloys ($ZnFe_2O_4$, $MnFe_2O_4$, $NiFe_2O_4$) [4]. Superparamagnetic nanoparticles (SPIONs) are a specific category of magnetic nanoparticles, containing Fe_3O_4, $MnFe_2O_4$, Fe_2O_3, FeCo, etc, which can be controlled temporally and spatially by external magnetic fields. SPIONs have been used in different biomedical applications, such as drug delivery [34], targeted therapeutics [35] and medical imaging [36]. When the external magnetic field is removed, all the magnetic interactions of the nanoparticles disappear with the average net magnetization returning to zero. Studies have shown it is possible to infuse SPIONs into hydrogel inks for extrusion 3D printing to be used for magnetic actuation [37] and self-healing tissue scaffolds [38]. Another study has shown SPIONs could be formulated into photopolymerizable ink for 3D printing of magnetic micro-swimmers through two-photon polymerisation (2 P P), resulting in magnetic actuation, control and navigation [39]. However, due to the natural agglomeration and sedimentation of SPIONs in low viscosity photo-resins, resulting in inhomogeneous distribution, limitations arise when using DLP and SLA type printing.

There have been several methods to combine magnetic nanoparticles with 3D printing of hydrogels. The simplest is to create a mixture of SPIONs with photocurable monomers, crosslinkers and photoinitiators as photo-resin for printing. To achieve functional- and stimuli-response 3D printed hydrogels, the SPIONs must first be homogenously dispersed within the photo-resin prior to printing. Physical mixing and ultrasonication can be used for good dispersion and to prevent agglomeration of the SPIONs [32]. Surface modification methods such as coating [40,41] and grafting [42,43] of nanoparticles are also popular methods to achieve a homo-geneously mixed photo-resin. Another method includes grafting polymer chains onto the surface of nanoparticles to increase the distance between surrounding nanoparticles. This can provide repulsion forces when nanoparticles are in proximity, reducing the effects of agglomeration. Increasing the viscosity of the photo-resin will also prevent nanoparticles sedimentation during printing. Koboyashi et al. added a reagent to increase the viscosity of a magnetic photo-resin, resulting in a more stable and well dispersed mixture with effects lasting for ten days [44]. Xiong et al. used L-ascorbic acid as both a reducing and capping agent to prepare highly stable copper nanoparticles without agglomeration [45]. This was achieved by manipulating the zeta potential on the surface of the nanoparticles. Nanoparticles with high zeta potential (absolute value) show greater repulsion interaction between each other, leading to less aggregation and better stability in suspension [46]. Tang et al. infused hard NdFeB magnetic particles and milled freeze-dried microgels into a hydrogel precursor ink, resulting in a magnetic hydrogel with excellent mechanical properties and programmable actuation under an external magnetic field [47]. Additionally, controlling the alignment of magnetic nanoparticles during printing can enhance the hydrogels mechanical properties [48], energy landscape [49], response rate [50] and electrical properties. In one study, an external magnetic field was used to control the direction of magnetic nanoparticles within their magnetic alginate methylcellulose ink whilst printing hydrogel actuators [8]. This resulted in aligned orientation of pores and enhanced mechanical properties of their

actuators whilst remaining responsive to magnetic stimuli [8].

In this work, we aimed to develop a photo-resin that is homogeneously infused with SPIONs with reduced agglomeration during printing in order to print magnetically actuated hydrogels. The photo-resin is composed of acrylamide (AAm), polyethylene glycol diacrylate (PEGDA) and sodium L-ascorbate and is optimised for SLA. The resulting 3D printed starfish-shaped hydrogels exhibit strong superparamagnetic properties enabling them to respond to external magnetic stimuli and revert to their original shape once the stimuli are removed. The 3D printed hydrogels overcome the limitations of using traditional extrusion printing to print magnetic hydrogels, enabling more complex and delicate structures [22]. The printed hydrogels are soft and flexible, making them a promising material for a range of cutting-edge applications, ranging from soft robotic actuators and robotic swimmers to aquatic grabbers.

2. Materials and methods

2.1. Materials

Anhydrous iron (III) chloride (98% purity), iron (II) chloride tetrahydrate (98% purity), sodium hydroxide aqueous solution (1 M), hydrochloric acid aqueous solution (1 M), acrylamide (Aam, average M_w = 71.08, purity≥99%), Poly (ethylene glycol) diacrylate (PEGDA) (M_w~700, purity≥99%), lithium phenyl-2,4,6-trimethylbenzoylphosphinate (LAP) (≥95%), citric acid and sodium L-ascorbate were all purchased from Sigma-Aldrich (Dorset, UK).

2.2. Synthesis of superparamagnetic iron oxide nanoparticles (SPIONs)

50 mL of deionized water (DW) was mixed with 10 mL of 1 M HCl. Soon after, 3.25 g $FeCl_3$ and 2 g $FeCl_2{\cdot}4H_2O$ powders were dissolved in the acidic solution under vigorous stirring. The resulted iron ions solution was added dropwise into 100 mL of 1 M NaOH solution under continuous vigorous stirring while degassing the system with high purity argon gas (99.9%) [51]. The solution was kept under stirring for 30 min. The obtained black precipitate was washed 5 times with 50 mL deionized water to ensure all the unreacted reagents were removed. Then the prepared SPIONs were stored in DW solution (1400 μS/cm, at 25 °C) at concentration of 0.03 g mL^{-1}.

2.3. Characterization of SPIONs

SPIONs were analyzed using Fourier Transform-Infrared Spectroscopy (FTIR, Thermo scientific) to confirm their chemical composition. UV–visible spectroscopy (Lambda 25) was used to obtain the adsorption spectrum. The crystal structure was detected using an X-ray diffractometer (XRD, Bruker D2 Phaser instrument) with a copper X-ray tube at a power of 30 kV and 10 mA generator while $\lambda = 1.5418$ Å. XRD patterns were recorded in 2θ ranging from 20° to 80° with a step size of 0.034. X-ray photoelectron spectroscopy (XPS) was used to analyse the different oxidation states of iron in the SPIONs. The morphology and size of the SPIONs was examined using transmission electron microscopy (TEM, Jeol JEM-2100 F) and dynamic light scattering (DLS, Zetasizer NANO). The average size of the SPIONs was also determined by measuring the diameter of 100 nanoparticles TEM images using ImageJ software. The samples used in FTIR, XRD and XPS were in dried powder form. For UV–vis and DLS, small amounts of SPION powder were dissolved in distilled water and ultrasonicated for 20 min until a transparent solution was achieved. For TEM, 20 mg of SPION powder was mixed with ethanol and ultrasonicated to break up agglomerates, and then droplets were placed onto a TEM grid. Dried SPION powder was sealed in a polycarbonate capsule with wool for testing using the Superconducting Quantum Interference Device (SQUID).

2.4. Preparation of SPION-infused photo-resin and 3D printed starfish

1 M stock solution was prepared by adding 4.95 g sodium L-ascorbate and 5.25 g citric acid to 25 mL distilled water. Citric acid and sodium L-ascorbate amounts were calculated based on total weight of monomers and crosslinkers. The calculated amount of acrylamide, PEGDA, lithium phenyl-2,4,6-trimethylbenzoylphosphinate, distilled water and citric acid solution/sodium L-ascorbate solution were added to a pot and stirred for 5 min (Table 1). A total of 50 g of photo-resin per formulation was made. The magnetic stirrer was taken out and the SPION solution was added. SPION concentration was calculated relative to the total mass of monomers and crosslinkers. The photo-resin mixture was put into ultrasonic bath for 20 min before being poured into a Formlabs Form 2 SLA printer (405 nm, 250 mW light source) tank to print under 'Open Mode' using 'Clear Resin' settings and 100 μm layer height. The CAD models were uploaded using Preform and the print was started immediately.

Table 1
Trial formulations of 3D printing photo-resin for optimization. 1 M of Citric acid and Sodium L-ascorbate was used, calculated in terms of total mass of monomers and crosslinkers. The photoinitiator LAP, and SPIONs was calculated in terms of total mass of the monomers and crosslinkers. Each formulation was made up to a total mass of 50 g.

Formulation	Acrylamide wt%	PEGDA wt%	LAP wt%	Water wt%	SPIONs wt%	Citric acid solution %	Sodium L-ascorbate solution %
1	15	5	1	80	0.1	1	0
2	15	5	1	80	0.1	0	1
3	15	5	1	80	0.1	0.5	0.5
4	20	10	1	70	0.1	0.7	0

In the process of printing (Fig. 1), the photo-resin was mixed manually every 5 layers to avoid bubbles caused by the build platform and any potential agglomeration or sedimentation of SPIONs in the resin tank. Bubbles were not noticeable after the first 10 layers and sedimentation was minimal. When printing was completed, the build-platform was detached from printer and residual photo-resin was carefully washed off using distilled water. The printed hydrogels were removed from platform using a thin string while continuously being rinsed lightly with distilled water. Once detached, the hydrogels were put into a container of water and post-cured using a Formlabs Form Cure for 10 min at room temperature.

2.5. Characterization of 3D printed starfish

The chemical bonds of the 3D printed SPION-infused hydrogels were detected through FTIR spectroscopy. The morphology of the hydrogels was imaged using SEM (Joel JSM-6010PLUS/LA) with WD = 7–8 mm under 20 kV voltage.

For FTIR, 3D printed hydrogels were cut into small pieces and dried at 60 °C overnight to remove water. Prior to SEM imaging, 3D printed hydrogels were cut into cross sections and freeze dried for 48 h. Freeze dried samples were then mounted on SEM holders with sample cross-section facing up and sputter coated with a thin layer of gold. Cylindrical SPION-infused hydrogels with 12 mm diameter and 10 mm height were 3D printed for compression tests. The diameter and height of each cylinder was measured before being subjected to compression testing. Compression tests were conducted using a Zwick Roell Z010 machine with 10 kN load cell at a speed of 1.5 mm min^{-1}. The force was applied perpendicular to the sample. The test was stopped at the first appearance of a steep reduction in force, indicating mechanical failure of the hydrogel. The displacement-load curves were plotted to determine the compression strength and Youngs Modulus. 3D printed cylindrical hydrogels with 0.5 wt% and 1 wt % were swollen for 48 h until they reached a plateau in weight prior to mechanical testing. For swelling measurements, 3D printed cylindrical hydrogels with 12 mm diameters and 10 mm heights were measured in weight before and after being submerged in distilled water for 72 h in sealed containers. Excess water was removed before weighing. The swelling degree (SD) by weight can be calculated as Eq. (1).

$$swelling\ degree = \frac{m_{wet} - m_{dry}}{m_{dry}} \times 100\% \quad (1)$$

Where m_{wet} is the weight of hydrogel after swelling and m_{dry} is the weight of hydrogel before swelling. The swelling degree of volume is calculated in the same manner.

3. Results and discussion

3.1. SPIONs

The SPIONs were synthesized by following a co-precipitation of ferrous and ferric ions in a basic solution. TEM images in Fig. 2a show the morphology of synthesized SPIONs. Images indicate that SPIONs tend to form clusters with particles ranging in size from approximately 18 nm to less than 10 nm, with an average diameter of 11 ± 3.5 nm (n = 100). The SPIONs aggregation phenomenon could be explained by their average hydrodynamic size in water at pH 8.63 (Fig. 2c). Their polydispersity index (PDI) of 0.342 indicates moderate polydispersity. The DLS curves show two significant peaks at 67 nm and 260 nm indicating single or small clusters of

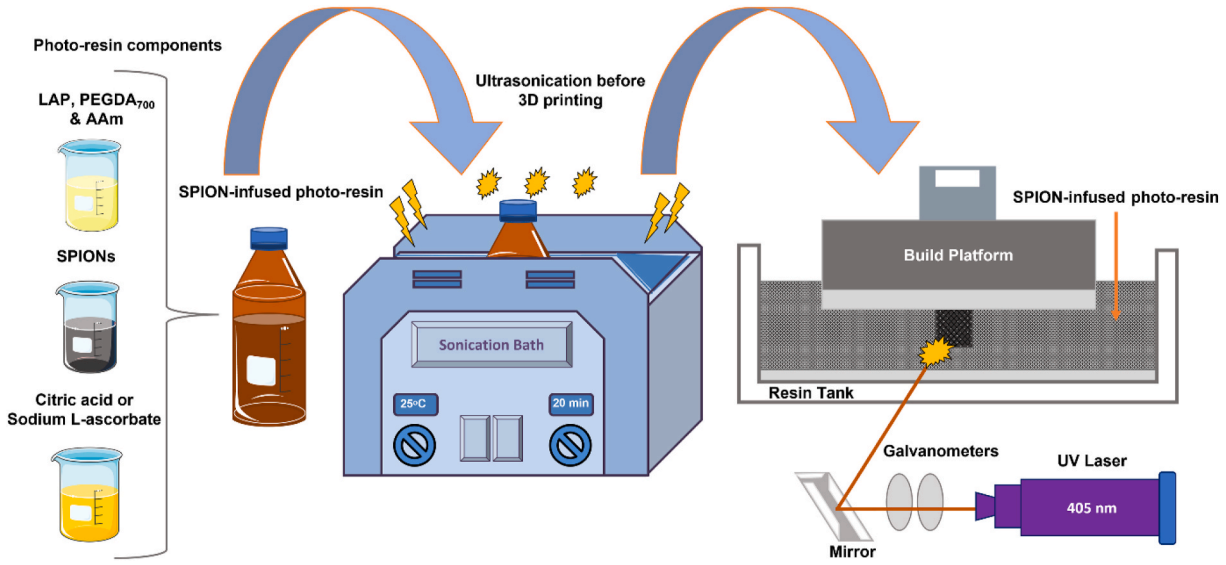

Fig. 1. Schematic figure of the 3D printing procedure of SPION-infused hydrogels.

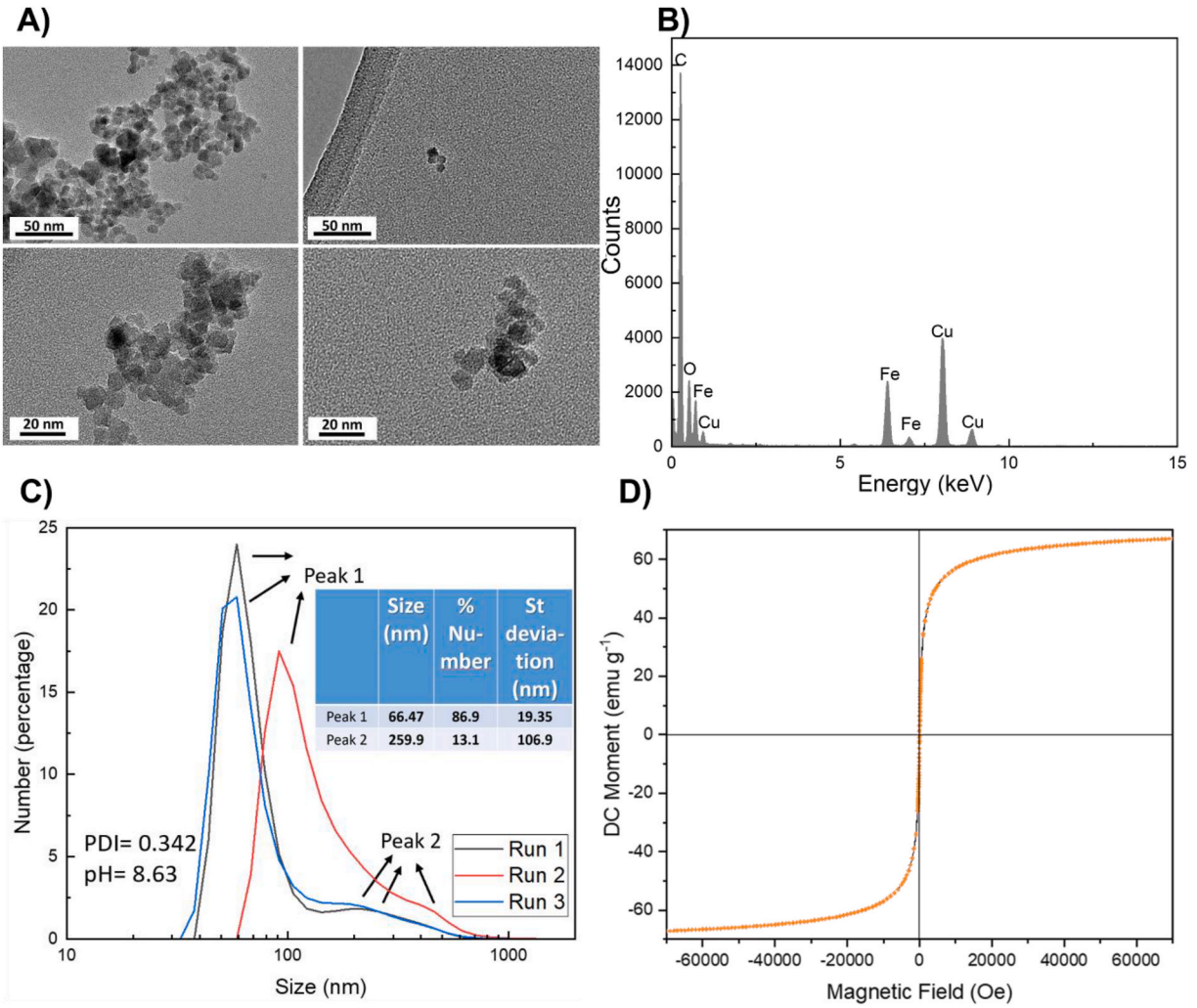

Fig. 2. Characterization of synthesized SPIONs showing morphology and size distribution, chemical makeup and superparamagnetic properties of the SPIONs, by: A) TEM; B) EDX elemental analysis; C) DLS size distribution curves by number percentage and average size values in table after three runs under the same condition. The arrows indicate the regions of Peak 1 and Peak 2 for each run; D) Room temperature SQUID.

SPIONs, as well as larger clusters, respectively, highlighted with arrows indicating Peak 1 and Peak 2 in Fig. 2c. Moreover, a zeta potential value of −8.07 mV indicates that the SPIONs lacked enough surface charge to prevent agglomeration in water and had low colloidal stability. The energy dispersive spectroscopy (EDS) spectrum in Fig. 2b shows the elemental composition of SPIONs, confirming the presence of iron and oxygen. The absence of sodium and chlorine indicates a high purity, with no reagent residue. The copper peak is due to the grid composition. The strong superparamagnetic property of SPIONs is reported in Fig. 2d. The hysteresis curve shows symmetry in terms of zero axes, depicting typical superparamagnetic behaviour [52]. At room temperature, the curve is entirely reversible and without any hysteresis. The saturation magnetization of synthesized SPIONs is 67 emu g^{-1} according to this curve, which shows a super strong signal. The SPIONs composition was also investigated by FTIR spectroscopy. Fig. 3a shows the SPIONs with a broad adsorption band exists at 3400-3500 cm^{-1}, corresponding to the presence of surface hydroxyl groups (Fe–OH) [53]. The presence of Fe–OH on the SPION surface is due to a spontaneously proton transfer from the aqueous phase to the SPION surface [54]. The two strong adsorption at around 615 cm^{-1} and 536 cm^{-1} can be assigned to maghemite, indicating that maghemite existed in synthesized iron oxides mixture [55]. The UV–vis spectrum of SPIONs in Supplementary information (Fig. S1) show two peaks at 327 nm and 384 nm, which are characteristic features of two crystalline structures in iron oxides with different oxidation states of iron. To further investigate SPIONs composition, XRD and XPS were performed. Fig. 3b shows the XRD pattern of the SPIONs with characteristic peaks assigned to (220), (311), (400), (422), (511), and (440) planes respectively, all of which attributed to both Fe_3O_4 and γ-Fe_2O_3 [51]. The calculated composition by weight is 72.36% iron and 27.64% oxygen, indicating that magnetite dominates the mixture. According to the Debye Scherrer equation Eq. (2) [56].

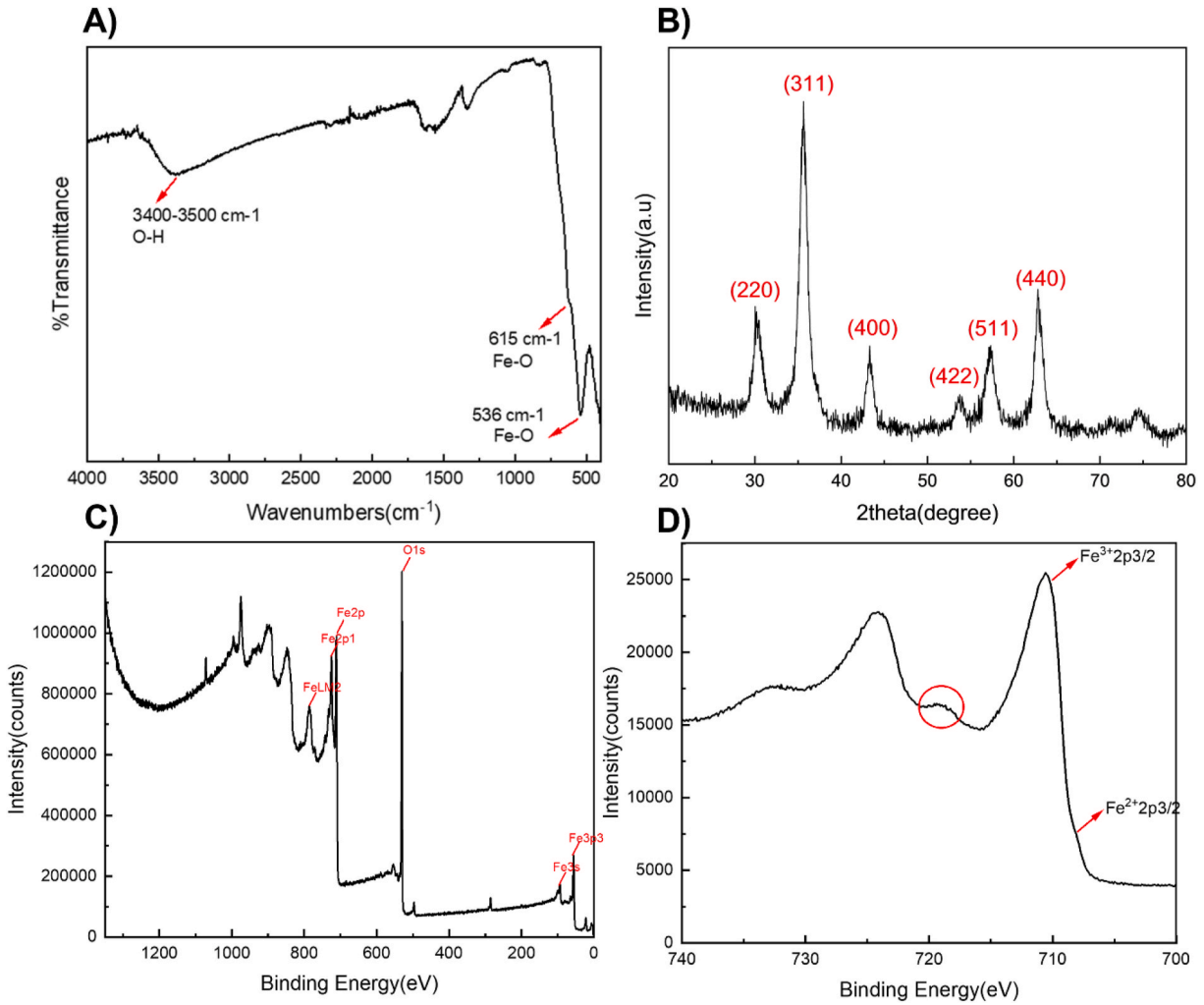

Fig. 3. Characterization of synthesized SPIONs: A) FTIR spectrum; B) XRD diffraction pattern; C) XPS survey spectrum; D) XPS Fe2p scan spectrum.

$$D = \frac{k\lambda}{\beta \cos \theta} \tag{2}$$

Where k is the Scherrer constant which is usually taken as 0.9 [57], λ is the wavelength of the X-ray beam in the machine (1.541 Å), β is the Full width at half maximum (FWHM) of the peak and θ is the Bragg angle of the determined peak, the calculated average particle of SPIONs based on two strong peaks (311) and (220) was 14.6 nm. This result is in accordance with the calculated SPIONs size measured by TEM. The presence of both magnetite and maghemite in the SPIONs was confirmed by detecting the two different oxidation states of iron oxide. The X-ray photoelectron spectrum in Fig. 3c shows sharp and strong peak at 530 eV which belongs to oxygen, while two series of peaks from 825 eV to 700 eV and 110 to 45 eV correspond to the different binding energy in Fe on the surface of sample. From the Fe2p scan spectrum in Fig. 3d, it is noted that a small peak at 709 eV which belongs to $Fe2^{+}2p3/2$, overlaps with the high peak of $Fe3^{+}2p3/2$ at 711 eV. When comparing the similar standard Fe2p spectrums of magnetite and maghemite, one small characteristic band ranging from 721 eV to 717 eV appears in the maghemite spectrum only, which can be used to distinguish them [58]. The presence of this small band in Fig. 3d (red circle) confirms the existence of maghemite in synthesized SPIONs mixture. According to the peak analysis in XPS, the atomic composition percentage was 46.37% iron and 49.47% oxygen. The atomic percentage in Fe_2O_3 should be 42.9% Fe and 57.1% O while 40% Fe and 60% O exist in Fe_3O_4. The slightly higher atomic ratio that Fe element shared in XPS samples may be attributed to the existence of FeOH on the SPIONs surface.

3.2. Photo-resin optimization and 3D printed starfish

Photo-resin formulations were optimised to achieve optimal hydrogel homogeneity and mechanical stability after swelling in water, and the ability to return to their original shape once the magnetic stimuli was removed. The base composition of the photo-resin

was 15 wt% acrylamide (monomer); 5 wt% PEGDA (crosslinker), 1 wt% LAP (photoinitiator) and 80 wt% water. Varying amounts of SPIONs solution were added directly to the photo-resin. However, SPIONs began to agglomerate due to local magnetic fields in the printer caused by magnets in the corners of lid that help ensure the printer is sealed during printing. This resulted in nanoparticle interactions and sedimentation during printing. This caused a poor distribution of SPIONs during initial trials (Fig. S2 in Supplementary information). Maghemite and magnetite have different oxidation states of Fe ion. The amount of Fe ions with different charges on the surface of SPIONs may influence the zeta potential to a large degree [59]. Previous work has shown a one-step precipitation method using citric acid can increase the zeta potential and hydrophilicity of the SPIONs surface [60]. Therefore, citric acid and sodium L-ascorbate were trialled in this work to improve SPION dispersion within the photo-resins (Table 1). Bulk samples were prepared in moulds during the optimization process until a final formulation with homogenous SPIONs distribution was achieved (Fig. 3a SI). Bulk hydrogels with the addition of citric acid (Table 1, formulation 1) exhibited the optimal SPION homogeneity. However, incomplete photo-curing was exhibited in the inner bulk of formulation 1. Thus, the crosslinker ratio was increased (Table 1, Formulation 4) to ensure complete crosslinking and physically stable mechanical properties. The final three photo-resin formulations shown in Table 2 with 0.5 wt%, 1 wt% and 2 wt% SPIONs respectively exhibited the best performance during printing and were used in this study. Reduced print duration resulted in improved homogeneity of the hydrogel as the probability of sedimentation increases with time. Thinner hydrogels require lower print durations and can react faster with more precise control under a magnetic field. For these reasons, two starfish models were designed with thicknesses of 3.8 mm and 2 mm each. Fig. 4a–d shows the CAD designs and images of the 3D printed hydrogel starfish on the build platform. The two different CAD models shown in Fig. 4a featured spaces between each segment of the arms to allow more flexible movement during magnetic actuation. However, due to overcuring caused by potential light-scattering from the SPIONs, refraction at early print layers off the platform, and without the addition of a light-absorber [61–63], those features were not completely achieved. The increase in light scattering causes more photo-resin around the laser beam to cure, therefore, the curing width is increased, leading to the limited print resolution. Future mitigation is needed to counter these effects, such as photo-absorbers [33].

The chemical composition of the 3D printed hydrogels with 0.5 wt%, 1 wt% and 2 wt% SPIONs was examined using FTIR (Fig. 4e). The strong band at 472 cm^{-1} represents the Fe–O bond in magnetite and maghemite, showing a slight shift to smaller wavenumbers as compared to the spectrum of SPIONs in Fig. 2a, which is attributed to the combination of acrylamide-PEGDA network and SPIONs. The *N*–H stretching at 3337 cm^{-1}, the C═O at 1650 cm^{-1} and the NH_2 1091 cm^{-1} are assigned to the PEGDA-acrylamide hydrogel chemical network. It is noted that FTIR bands of polymer hydrogel matrix with three SPIONs concentrations exhibited a good agreement, indicating that the chemical structure of the hydrogel phase was not impacted by the increase of SPIONs concentration.

The structure of 3D printed hydrogels is shown in the SEM images in Fig. 5a–c. All samples show the commonly exhibited characteristic porous walls of freeze-dried hydrogels [11,12,16]s. Due to the layer-by-layer build, the resulting hydrogels exhibit a laminar structure in their cross-section. By comparing Fig. 5a, b and c, it is evident that increasing the SPION concentration results in more densely packed polymer networks. Samples with 2 wt% SPIONs have more noticeable agglomeration within the polymer strands (Fig. 5c). However, this agglomeration did not impact the hydrogels' ability to respond to a magnetic field and response to stimuli across the starfish arms was visibly uniform [64to67].

The application of magnetic hydrogels in soft robotic actuators requires stable mechanical deformation during swelling, before and after magnetic actuation, and robust mechanical properties must be achieved to extend product service life and avoid breakage [68]. Compression tests were carried out on cylinder samples with 0.5 wt% and 1 wt% SPIONs to study the impact of the nanocomposite structure on mechanical properties. Hydrogels with 2 wt% SPIONs did not yield sufficient print samples for testing due to rapid agglomeration during the printing process. Compression curves are shown in Fig. 5d and e. For each curve, the compression strength and final deformation values were taken from the highest point before samples exhibited a rapid decline in stress indicating failure. Fig. 5f shows similar average deformation values for 0.5 wt% and 1 wt% SPION-infused hydrogels of ~29%. The average compression strength of 0.5 wt% SPIONs hydrogel was 577 ± 96 kPa, more than twice the value for 1 wt% hydrogels at 255 ± 35 kPa. The Youngs modulus reflected a similar trend, 1838 ± 420 kPa for 0.5 wt% SPIONs hydrogel and 834 ± 46 kPa for 1 wt% samples. The mechanical performance of hydrogels with 0.5 wt % SPIONs is comparable to a previously reported alginate hydrogel composite embedded with Fe_3O_4 nanoparticles, showing a relatively higher compression stress but lower Youngs modulus [8]. Higher concentration of SPIONs results in fewer crosslinking points within the polymer network, preventing the formation of longer polymer chains and decreased crystallinity [67]. Additionally, more agglomeration occurs at higher concentrations of SPIONs that can result in poor homogeneity of the hydrogels, contributing to a reduced load-bearing capacity.

Among the various applications of soft actuators, soft robotics are increasingly utilised in aquatic environments [69]. Therefore, to carry out tasks successfully under water, such as transport of small cargo, or micro robotics for vascular operations [70], the hydrogel must exhibit swelling behaviour that maintains the materials structural integrity and limits size deformation, as well as respond to stimuli in water or aqueous solutions. Fig. 6d shows the swelling degree by weight and by change of dimensions of the printed

Table 2
Optimised photo-resin formulations. 1 M of Citric acid was used, calculated in terms of total mass of monomers and crosslinkers. The photoinitiator LAP was calculated in terms of total mass of the monomers and crosslinkers. Each formulation was made up to a total mass of 50 g.

Formulation	Acrylamide wt%	PEGDA wt%	LAP wt%	Water wt%	SPIONs wt%	Citric acid solution %
5	20	10	1	70	0.5 wt	0.88
6	20	10	1	70	1 wt	1.76
7	20	10	1	70	2 wt	3.53

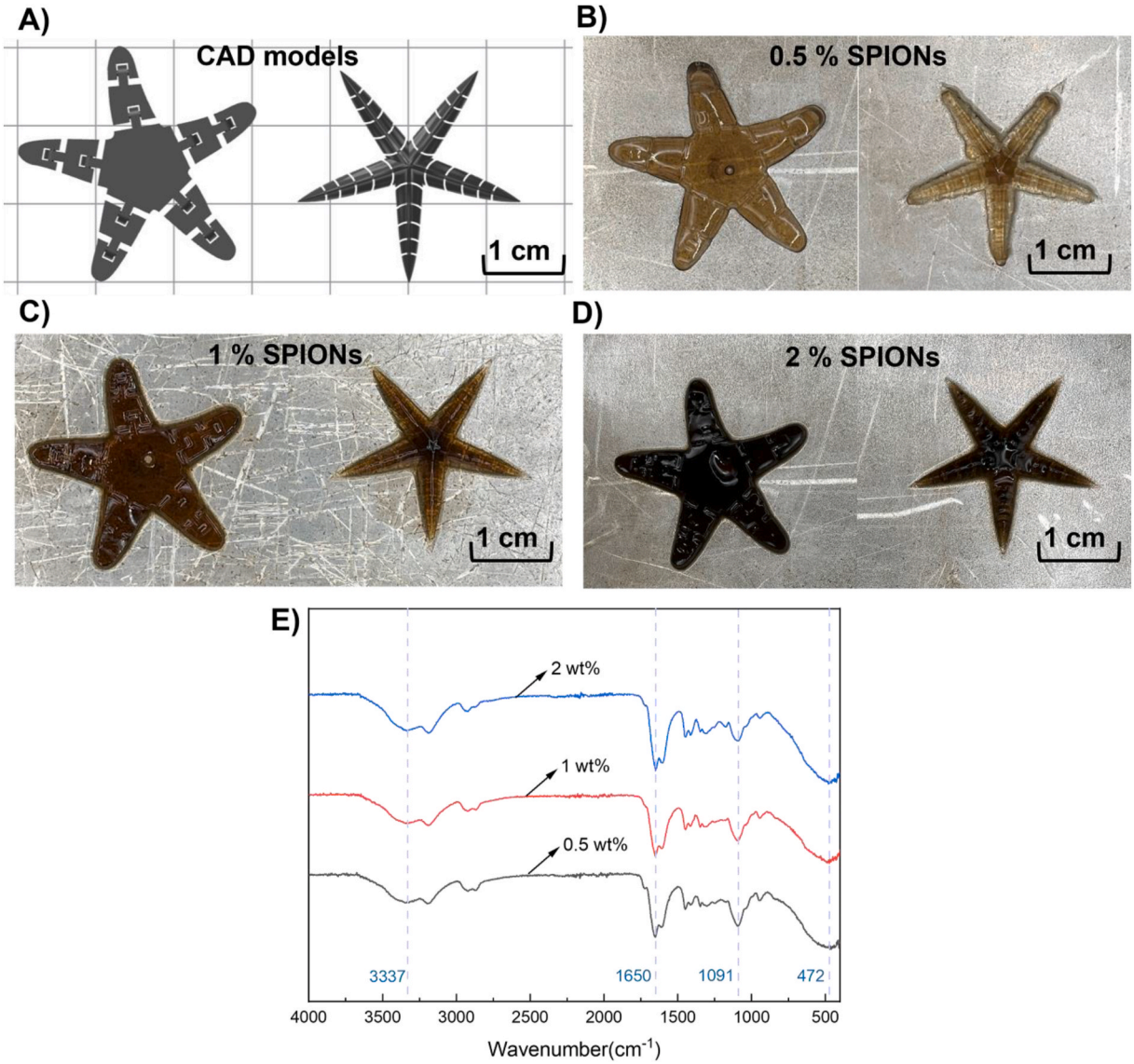

Fig. 4. A) Starfish CAD used for 3D printing; b-d) 3D printed starfish with varying SPION concentrations; e) FTIR spectra of 3D printed hydrogels with varying SPION concentrations.

cylindrical hydrogels after being submerged in distilled water for 72 h. The images of the hydrogel before and after swelling are compared in Fig. 6a and b. The CAD model used to 3D print the hydrogels is shown in Fig. 6c. Overall, the hydrogels with 0.5 wt% SPIONs possess a better capacity of up taking water than 1 wt% samples whilst their swelling degree by weight is higher than the swelling degree by volume for each concentration. The swelling degrees by weight of both concentrations are much lower than that in a previous study on a similar hydrogel composite containing Fe_3O_4 nanoparticles in polyacrylamide network [71], which reached 12,9% swelling capacity at its highest. This is probably a result of the addition of other hydrophilic components such as hydroxypropyl methylcellulose into the hydrogel network which can absorb more water, relatively. Hydrogels in this study are more stable than previously reported hydrogels [71], and have better control over water uptake, resulting in low deformation when swelling. As previously discussed, higher concentration of SPIONs inhibit the formation of long polymer chains. The obtained rigid and dense hydrogel network prevents water molecules to diffuse into the internal part. On the contrary, polymer networks composed of longer chains are susceptible to water absorption. Mechanical parameters and swelling degrees of hydrogels with 0.5 wt% and 1 wt% SPIONs are reported in Table 3.

To demonstrate the response of the 3D printed starfish under a magnetic field, a N42 magnet was used to induce movement. Stimuli response tests were conducted in water and recorded. As seen in Fig. 7a, the printed arms of hydrogel starfish with 1 wt% SPIONs were very flexible, swinging towards the magnet one by one and lifting itself up to attach to the magnet in a vertical response. Fig. 7b shows the horizontal response of the starfish to the magnet across the water bath. The starfish reacted quickly to the magnetic stimuli when

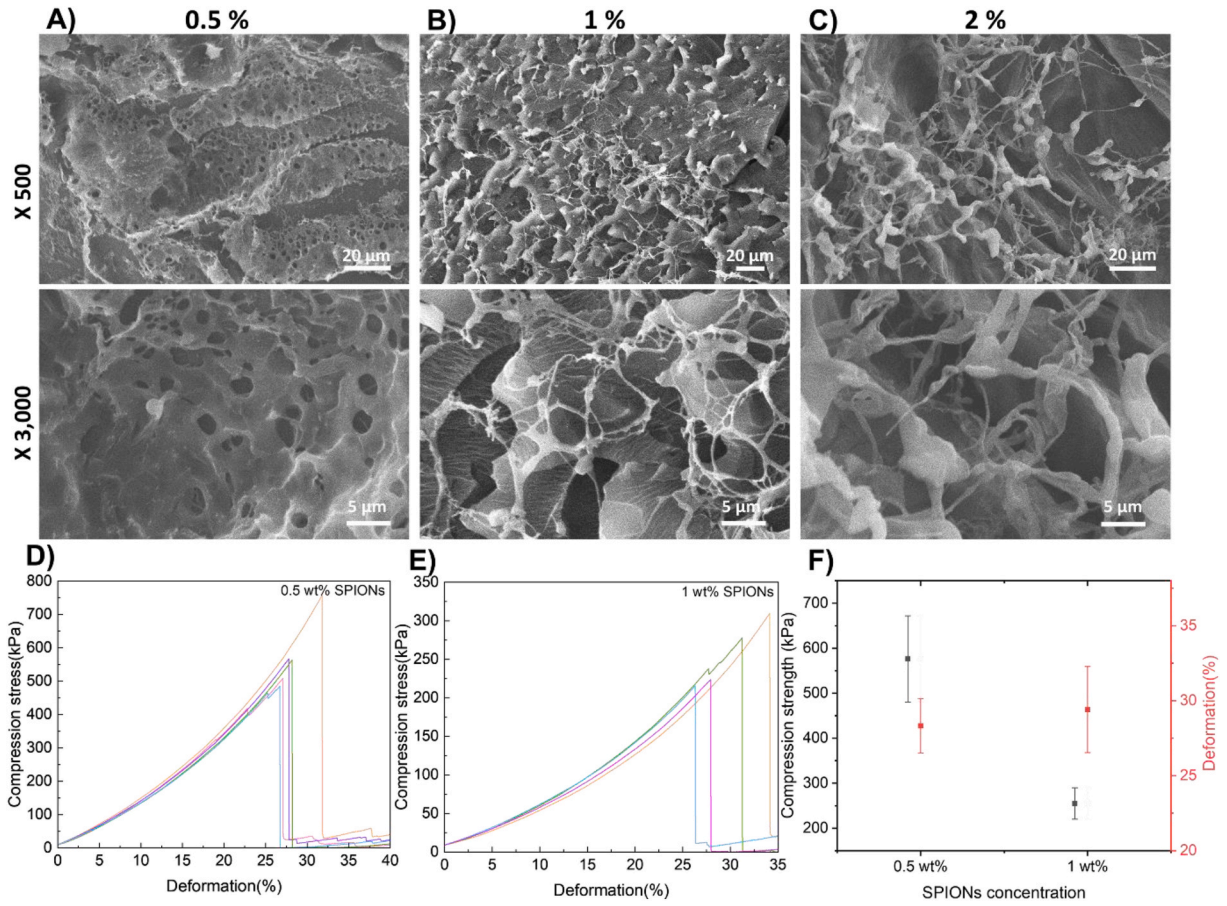

Fig. 5. Characterization of 3D printed starfish: a-c) SEM images of hydrogel with different SPIONs concentrations and at different magnifications; d) & e) 5 times deformation-load curves of printed cylindrical hydrogel with different SPIONs concentration; f) Average compression strength and relative % deformation.

the magnet was pressed against the outside of the glass walls of the water bath. Once the magnet was removed away from the water bath, the starfish returned to its original physical state. This is a representation of the inherit superparamagnetic behaviour of the SPION-infused 3D printed hydrogels, which show great potential for real-time control using external magnetic field. It is important to highlight that due to the superparamagnetic properties, the starfish were able to return to their original physically and old fold when in contact with a magnetic stimulus. Importantly, this allows a 'hold and release' action when used in direct applications such as micro cargo carriers or microgrippers. Further, the change in physical formation of the starfish did not result in any visible breakage, tearing or cracks before and after stimulation. The tested starfish model had a thickness of 3.8 mm. Test samples with 0.5 mm thickness using the same printing design model presented faster actuation and more precise spatial control in response to the magnet, which can be seen in Video 1 and Video 2 in the Supplementary Information.

4. Conclusions

This work has demonstrated the successful use of VAT polymerisation to achieve flexible, magnetic stimuli responsive starfish-shaped hydrogels as opposed to conventional extrusion-based printing techniques. A mixture of magnetite and maghemite nano-particles were successfully synthesized using a co-precipitation method resulting in superparamagnetic properties, with a saturation magnetization of 67 emu g-1. Achieving good dispersion and homogeneity of SPIONs in photo-resins can be challenging. This can be due to interactions between the particles and photo-resin because of surface charges that can result in sedimentation and/or agglomeration during 3D printing. In this study, these effects have successfully been reduced.

- Citric acid was used as a stabilising agent to reduce SPION agglomeration, as well as sedimentation, and improve homogeneity within the photo-resin. This resulted in better dispersed SPIONs in the final 3D printed structures.
- Photo-resin formulations containing 0.5 wt%, 1 wt% and 2 wt% SPIONs were achieved, with 0.5 wt % and 1 wt% as the optimal working concentrations for 3D printing. These two concentrations were used to 3D print starfish and cylinders, whereas 2 wt% SPION concentrations were limited to starfish due to increased agglomeration.

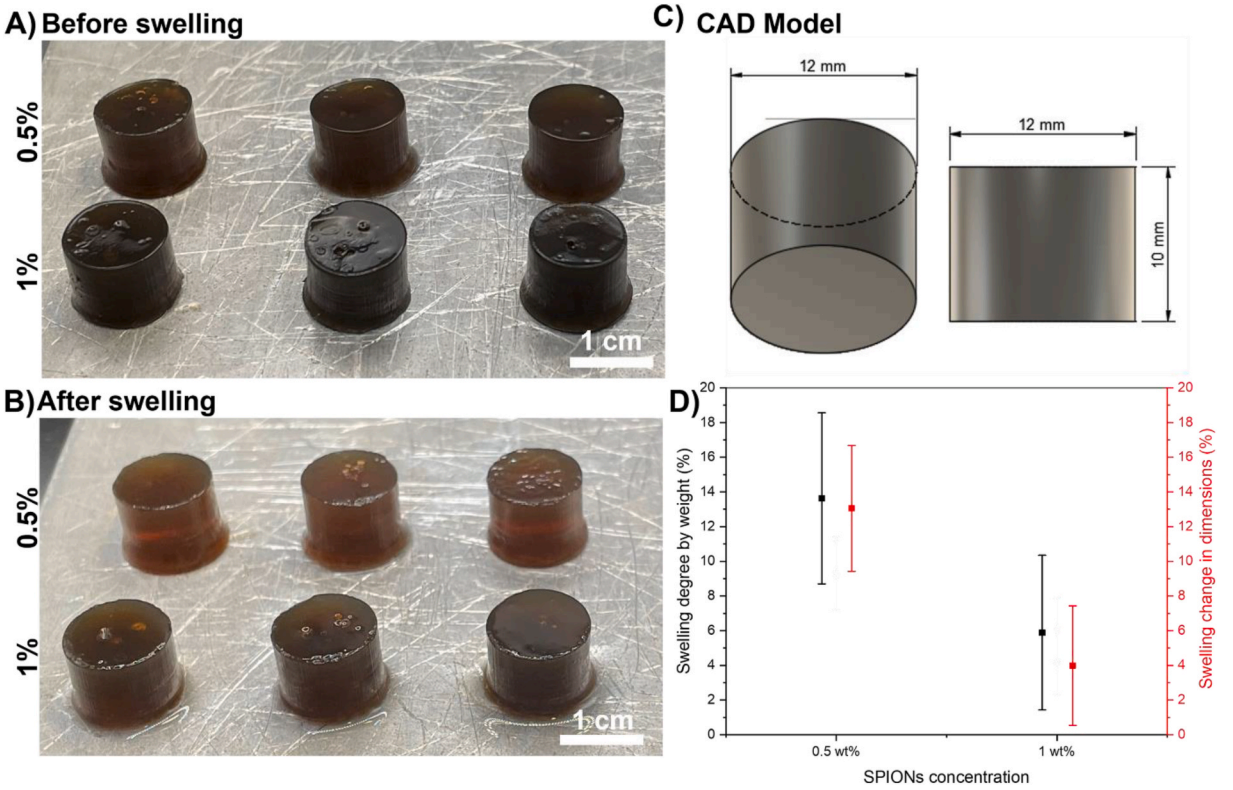

Fig. 6. A-b) 3D printed cylindrical SPION-infused hydrogels with 0.5 wt% and 1 wt% SPIONs before and after swelling; c) CAD models used for printing; d) Swelling degrees by weight and volume of printed cylindrical hydrogel composite.

Table 3
Comparison of mechanical properties and swelling properties between 3D printed hydrogel composites containing 0.5 wt% and 1 wt% SPIONs.

SPIONs	Compression strength (kPa)	Deformation under stress (%)	Youngs modulus (kPa)	Swelling degree by weight (%)	Swelling degree by volume (%)
0.5 wt%	577 ± 96	28 ± 2	1838 ± 42	9.3 ± 2.1	9.2 ± 2
1 wt%	255 ± 35	29 ± 3	834 ± 46	6 ± 1.9	4.2 ± 1.9

- Mechanical properties showed a decreasing trend with increased SPION concentration, with approximately 600 kPa compression stress for 0.5 wt% SPIONs hydrogel and 250 kPa for 1 wt% likely due to a disruption of the polymer network.
- The 3D printed starfish shaped hydrogels exhibited fast magnetic responsivity and flexible actuation, with original-shape retention and material stability once the external stimulus was removed.
- Ultimately, citric acid helped reduce agglomeration for the lower SPION concentrations, however, further work is required to increase the stability of a monodisperse solution including other trials with other capping agents such as oleic acid, or the addition of capping agents during SPION synthesis.

The use of this optimised procedure for VAT polymerisation will result in great opportunities in soft robotics and bioengineering, particularly with the benefits of superparamagnetic properties and high-resolution printing of small-scale structures. Specific applications requiring such systems include small cargo transport in aquatic environments, grabbing and manipulation in soft robotics, and in vivo applications such as targeted therapeutics and minimally invasive interventional microsurgery. The SPION-infused hydrogels reported here may be extended to other types of magnetic nanoparticles and hydrogels formulations, as well as other micro grabber designs. Finally, the methodology in this work can be applied to other types of nanoparticles for optimising the homogeneity and dispersion in water-based photo-resins.

Author contribution statement

Ali Mohammed, Alessandra Pinna: Conceived and designed the experiments; Performed the experiments; Analyzed and interpreted the data; Contributed reagents, materials, analysis tools or data; Wrote the paper.

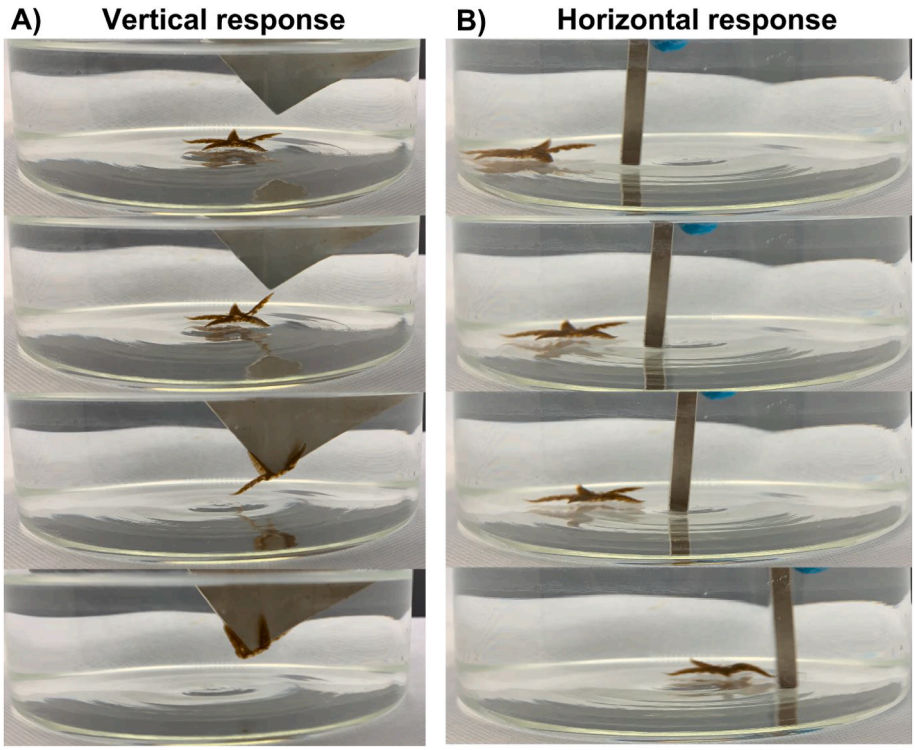

Fig. 7. Photos of 3D printed magnetic starfish hydrogels with 1 wt% SPIONs demonstrating response to a magnet. a) The arms swing towards the magnet and attach to it. b) Hydrogel starfish can follow the movement of the magnet. Related videos are shown in the Supplementary Information Video 3 and Video 4.

Jingqi Miao: Performed the experiments; Analyzed and interpreted the data; Wrote the paper.
Ieva Ragaisyte: Analyzed and interpreted the data.
Alexandra Porter, Connor Myant: Contributed reagents, materials, analysis tools or data.

Funding statement

This research did not receive any specific grant from funding agencies in the public, commercial, or not-for-profit sectors.

Data availability statement

Data will be made available on request.
Declaration of interest's statement.
The authors declare no conflict of interest.

Declaration of competing interest

The authors declare that they have no known competing financial interests or personal relationships that could have appeared to influence the work reported in this paper. The authors declare the following financial interests/personal relationships which may be considered as potential competing interests.

Acknowledgments

AM and JM share first-authorship equally.
This work is supported by Imperial College Research Fellowship scheme (2019–2023), Seeds for Success Grant (2021) from the Postdoc and Fellows Development Centre Imperial College London.

Appendix A. Supplementary data

Supplementary data to this article can be found online at https://doi.org/10.1016/j.heliyon.2023.e14682.

References

[1] A. Zolfagharian, A.Z. Kouzani, S.Y. Khoo, I. Gibson, A. Kaynak, 3D Printed Hydrogel Soft Actuators, in: IEEE Region 10 Conference (TENCON), 2016, pp. 2272–2277, 2016.
[2] M. Javadi, Q. Gu, S. Naficy, S. Farajikhah, J.M. Crook, G.G. Wallace, S. Beirne, S.E. Moulton, Conductive tough hydrogel for bioapplications, Macromol. Biosci. 18 (2) (2018), 1700270.
[3] L. Han, L. Yan, M. Wang, K. Wang, L. Fang, J. Zhou, J. Fang, F. Ren, X. Lu, Transparent, adhesive, and conductive hydrogel for soft bioelectronics based on light-transmitting polydopamine-doped polypyrrole nanofibrils, Chem. Mater. 30 (16) (2018) 5561–5572.
[4] S. Ganguly, S. Margel, 3D printed magnetic polymer composite hydrogels for hyperthermia and magnetic field driven structural manipulation, Prog. Polym. Sci. 131 (2022), 101574.
[5] Y.S. Lui, W.T. Sow, L.P. Tan, Y. Wu, Y. Lai, H. Li, 4D printing and stimuli-responsive materials in biomedical aspects, Acta Biomater. 92 (2019) 19–36.
[6] E. Sachyani Keneth, A. Kamyshny, M. Totaro, L. Beccai, S. Magdassi, 3D printing materials for soft robotics, Adv. Mater. 33 (19) (2021), 2003387.
[7] S.Y. Zheng, Y. Shen, F. Zhu, J. Yin, J. Qian, J. Fu, Z.L. Wu, Q. Zheng, Programmed deformations of 3D-printed tough physical hydrogels with high response speed and large output force, Adv. Funct. Mater. 28 (37) (2018), 1803366.
[8] D. Podstawczyk, M. Nizioł, P. Szymczyk, P. Wiśniewski, A. Guiseppi-Elie, 3D printed stimuli-responsive magnetic nanoparticle embedded alginate-methylcellulose hydrogel actuators, Addit. Manuf. 34 (2020), 101275.
[9] A.S. Hoffman, Hydrogels for biomedical applications, Adv. Drug Deliv. Rev. 64 (2012) 18–23.
[10] T.R. Hoare, D.S. Kohane, Hydrogels in drug delivery: progress and challenges, Polymer 49 (8) (2008) 1993–2007.
[11] A.A. Mohammed, A. Pinna, S. Li, T. Sang, J.R. Jones, Auto-catalytic redox polymerisation using nanoceria and glucose oxidase for double network hydrogels, J. Mater. Chem. B 8 (14) (2020) 2834–2844.
[12] A.A. Mohammed, J. Aviles Milan, S. Li, J.J. Chung, M.M. Stevens, T.K. Georgiou, J.R. Jones, Open vessel free radical photopolymerization of double network gels for biomaterial applications using glucose oxidase, J. Mater. Chem. B 7 (25) (2019) 4030–4039.
[13] J.L. Drury, D.J. Mooney, Hydrogels for tissue engineering: scaffold design variables and applications, Biomaterials 24 (24) (2003) 4337–4351.
[14] Z. Chen, Y. Chen, M.S. Hedenqvist, C. Chen, C. Cai, H. Li, H. Liu, J. Fu, Multifunctional conductive hydrogels and their applications as smart wearable devices, J. Mater. Chem. B 9 (11) (2021) 2561–2583.
[15] Z. Chen, J. Liu, Y. Chen, X. Zheng, H. Liu, H. Li, Multiple-stimuli-responsive and cellulose conductive ionic hydrogel for smart wearable devices and thermal actuators, ACS Appl. Mater. Interfaces 13 (1) (2021) 1353–1366.
[16] A.A. Mohammed, N.G. Merrild, S. Li, A. Pinna, J.R. Jones, Double-Network Hydrogels Reinforced with Covalently Bonded Silica Nanoparticles via 1-Ethyl-3-(3-Dimethylaminopropyl)carbodiimide Chemistry, ACS Omega, 2022.
[17] A.P. Constantinou, G. Patias, B. Somuncuoğlu, T. Brock, D.W. Lester, D.M. Haddleton, T.K. Georgiou, Homo- and co-polymerisation of di(propylene glycol) methyl ether methacrylate – a new monomer, Polym. Chem. 12 (24) (2021) 3522–3532.
[18] A.P. Constantinou, N.F. Sam-Soon, D.R. Carroll, T.K. Georgiou, Thermoresponsive tetrablock terpolymers: effect of architecture and composition on gelling behavior, Macromolecules 51 (18) (2018) 7019–7031.
[19] M.A. Ward, T.K. Georgiou, Thermoresponsive triblock copolymers based on methacrylate monomers: effect of molecular weight and composition, Soft Matter 8 (2012) 2737–2745.
[20] M.A. Ward, T.K. Georgiou, Multicompartment thermoresponsive gels: does the length of the hydrophobic side group matter? Polym. Chem. 4 (6) (2013) 1893–1902.
[21] E.M. Ahmed, Hydrogel: preparation, characterization, and applications: a review, J. Adv. Res. 6 (2) (2015) 105–121.
[22] J. Li, M. Pumera, 3D printing of functional microrobots, Chem. Soc. Rev. 50 (4) (2021) 2794–2838.
[23] A. Bagheri, J. Jin, Photopolymerization in 3D printing, ACS Appl. Polym. Mater. 1 (4) (2019) 593–611.
[24] G. Taormina, C. Sciancalepore, M. Messori, F. Bondioli, 3D printing processes for photocurable polymeric materials: technologies, materials, and future trends, J. Appl. Biomater. Funct. Mater. 16 (3) (2018) 151–160.
[25] F.P.W. Melchels, J. Feijen, D.W. Grijpma, A review on stereolithography and its applications in biomedical engineering, Biomaterials 31 (24) (2010) 6121–6130.
[26] T. Serra, J.A. Planell, M. Navarro, High-resolution PLA-based composite scaffolds via 3-D printing technology, Acta Biomater. 9 (3) (2013) 5521–5530.
[27] N. Palaganas, J. Mangadlao, A. de Leon, J. Palaganas, K. Pangilinan, Y. Lee, R. Advincula, 3D printing of photocurable cellulose nanocrystal composite for fabrication of complex architectures via stereolithography, ACS Appl. Mater. Interfaces 9 (2017).
[28] Q. Wang, J.A. Jackson, Q. Ge, J.B. Hopkins, C.M. Spadaccini, N.X. Fang, Lightweight mechanical metamaterials with tunable negative thermal expansion, Phys. Rev. Lett. 117 (17) (2016).
[29] Z. Katcharava, A. Marinow, R. Bhandary, W.H. Binder, 3D printable composite polymer electrolytes: influence of SiO2 nanoparticles on 3D-printability, Nanomaterials 12 (11) (2022) 1859.
[30] B. Baumann, T. Jungst, S. Stichler, S. Feineis, O. Wiltschka, M. Kuhlmann, M. Lindén, J. Groll, Control of nanoparticle release kinetics from 3D printed hydrogel scaffolds, Angew. Chem. Int. Ed. 56 (16) (2017) 4623–4628.
[31] S.Y. Song, M.S. Park, D. Lee, J.W. Lee, J.S. Yun, Optimization and characterization of high-viscosity ZrO2 ceramic nanocomposite resins for supportless stereolithography, Mater. Des. 180 (2019), 107960.
[32] J.Z. Manapat, Q. Chen, P. Ye, R.C. Advincula, 3D printing of polymer nanocomposites via stereolithography, Macromol. Mater. Eng. 302 (9) (2017), 1600553.
[33] Y. Yang, Z. Chen, X. Song, B. Zhu, T. Hsiai, P.-I. Wu, R. Xiong, J. Shi, Y. Chen, Q. Zhou, K.K. Shung, Three dimensional printing of high dielectric capacitor using projection based stereolithography method, Nano Energy 22 (2016) 414–421.
[34] B. Polyak, G. Friedman, Magnetic targeting for site-specific drug delivery: applications and clinical potential, Expet Opin. Drug Deliv. 6 (1) (2009) 53–70.
[35] S. Laurent, S. Dutz, U.O. Häfeli, M. Mahmoudi, Magnetic fluid hyperthermia: focus on superparamagnetic iron oxide nanoparticles, Adv. Colloid Interface Sci. 166 (1) (2011) 8–23.
[36] C.H. Cunningham, T. Arai, P.C. Yang, M.V. McConnell, J.M. Pauly, S.M. Conolly, Positive contrast magnetic resonance imaging of cells labeled with magnetic nanoparticles, Magn. Reson. Med. 53 (5) (2005) 999–1005.
[37] J. Simińska-Stanny, M. Nizioł, P. Szymczyk-Ziółkowska, M. Brożyna, A. Junka, A. Shavandi, D. Podstawczyk, 4D printing of patterned multimaterial magnetic hydrogel actuators, Addit. Manuf. 49 (2022), 102506.
[38] Y. Choi, C. Kim, H.S. Kim, C. Moon, K.Y. Lee, 3D Printing of dynamic tissue scaffold by combining self-healing hydrogel and self-healing ferrogel, Colloids Surf. B Biointerfaces 208 (2021), 112108.
[39] U. Bozuyuk, O. Yasa, I.C. Yasa, H. Ceylan, S. Kizilel, M. Sitti, Light-triggered drug release from 3D-printed magnetic chitosan microswimmers, ACS Nano 12 (9) (2018) 9617–9625.
[40] Y. Sahoo, H. Pizem, T. Fried, D. Golodnitsky, L. Burstein, C. Sukenik, G. Markovich, Alkyl phosphonate/phosphate coating on magnetite nanoparticles: a comparison with fatty acids, Langmuir 17 (2001) 7907–7911.
[41] M. Tajabadi, M.E. Khosroshahi, S. Bonakdar, An efficient method of SPION synthesis coated with third generation PAMAM dendrimer, Colloids Surf. A Physicochem. Eng. Asp. 431 (2013) 18–26.
[42] M. Takafuji, T. Mimaki, Z. Xu, H. Ihara, Surface charge controlled magnetic nanoparticles with grafting of poly(4-vinylpyridine), J. Nanosci. Nanotechnol. 5 (3) (2005) 390–393.
[43] A. Pinna, B. Lasio, D. Carboni, S. Marceddu, L. Malfatti, P. Innocenzi, Engineering the surface of hybrid organic–inorganic films with orthogonal grafting of oxide nanoparticles, J. Nanoparticle Res. 16 (7) (2014) 2463.
[44] K. Kobayashi, K. Ikuta, Three-dimensional magnetic microstructures fabricated by microstereolithography, Appl. Phys. Lett. 92 (26) (2008), 262505.
[45] J. Xiong, Y. Wang, Q. Xue, X. Wu, Synthesis of highly stable dispersions of nanosized copper particles using l-ascorbic acid, Green Chem. 13 (4) (2011) 900–904.
[46] T.L. Doane, C.-H. Chuang, R.J. Hill, C. Burda, Nanoparticle ζ -potentials, Acc. Chem. Res. 45 (3) (2012) 317–326.

[47] J. Tang, B. Sun, Q. Yin, M. Yang, J. Hu, T. Wang, 3D printable, tough, magnetic hydrogels with programmed magnetization for fast actuation, J. Mater. Chem. B 9 (44) (2021) 9183–9190.
[48] R. Libanori, R.M. Erb, A.R. Studart, Mechanics of platelet-reinforced composites assembled using mechanical and magnetic stimuli, ACS Appl. Mater. Interfaces 5 (21) (2013) 10794–10805.
[49] J.J. Martin, M.S. Riederer, M.D. Krebs, R.M. Erb, Understanding and overcoming shear alignment of fibers during extrusion, Soft Matter 11 (2) (2015) 400–405.
[50] D. Kokkinis, M. Schaffner, A.R. Studart, Multimaterial magnetically assisted 3D printing of composite materials, Nat. Commun. 6 (1) (2015) 8643.
[51] S. Yu, G.M. Chow, Carboxyl group (–CO2H) functionalized ferrimagnetic iron oxide nanoparticles for potential bio-applications, J. Mater. Chem. 14 (18) (2004) 2781–2786.
[52] H. Mamiya, B. Jeyadevan, Magnetic hysteresis loop in a superparamagnetic state, IEEE Trans. Magn. 50 (1) (2014) 1–4.
[53] T. Javanbakht, S. Laurent, D. Stanicki, W. Raphael, J.R. Tavares, Charge effect of superparamagnetic iron oxide nanoparticles on their surface functionalization by photo-initiated chemical vapour deposition, J. Nanoparticle Res. 17 (12) (2015) 462.
[54] E. Tombácz, K. Farkas, I. Földesi, M. Szekeres, E. Illés, I.Y. Tóth, D. Nesztor, T. Szabó, Polyelectrolyte coating on superparamagnetic iron oxide nanoparticles as interface between magnetic core and biorelevant media, Interfac. Focus 6 (6) (2016), 20160068.
[55] P. Tartaj, M.a.d.P. Morales, S. Veintemillas-Verdaguer, T. Gonz lez-Carre o, C.J. Serna, The preparation of magnetic nanoparticles for applications in biomedicine, J. Phys. Appl. Phys. 36 (13) (2003) R182–R197.
[56] A. Sundaresan, C.N.R. Rao, Ferromagnetism as a universal feature of inorganic nanoparticles, Nano Today 4 (1) (2009) 96–106.
[57] H.-I. Hsiang, C.-S. Hsi, C.-C. Huang, S.-L. Fu, Low temperature sintering and dielectric properties of BaTiO3 with glass addition, Mater. Chem. Phys. 113 (2) (2009) 658–663.
[58] A.P. Grosvenor, B.A. Kobe, M.C. Biesinger, N.S. McIntyre, Investigation of multiplet splitting of Fe 2p XPS spectra and bonding in iron compounds, Surf. Interface Anal. 36 (12) (2004) 1564–1574.
[59] U. Sakulkhu, M. Mahmoudi, L. Maurizi, G. Coullerez, M. Hofmann-Amtenbrink, M. Vries, M. Motazacker, F. Rezaee, H. Hofmann, Significance of surface charge and shell material of superparamagnetic iron oxide nanoparticle (SPION) based core/shell nanoparticles on the composition of the protein corona, Biomater. Sci. 3 (2) (2015) 265–278.
[60] M.A. Dheyab, A.A. Aziz, M.S. Jameel, O.A. Noqta, P.M. Khaniabadi, B. Mehrdel, Simple rapid stabilization method through citric acid modification for magnetite nanoparticles, Sci. Rep. 10 (1) (2020).
[61] G. Burke, D.M. Devine, I. Major, Effect of Stereolithography 3D Printing on the Properties of PEGDMA Hydrogels, Polymers, 2020.
[62] X.N. Zhang, Q. Zheng, Z.L. Wu, Recent advances in 3D printing of tough hydrogels: a review, Compos. B Eng. 238 (2022), 109895.
[63] B. Guo, Y. Zhong, X. Chen, S. Yu, J. Bai, 3D printing of electrically conductive and degradable hydrogel for epidermal strain sensor, Compos. Commun. 37 (2023), 101454.
[64] A. Jedlovszky-Hajdú, F.B. Bombelli, M.P. Monopoli, E. Tombácz, K.A. Dawson, Surface coatings shape the protein corona of SPIONs with relevance to their application in vivo, Langmuir 28 (42) (2012) 14983–14991.
[65] U. Maver, M. Bele, D. Makovec, S. Čampelj, J. Jamnik, M. Gaberšček, Incorporation and release of drug into/from superparamagnetic iron oxide nanoparticles, J. Magn. Magn Mater. 321 (19) (2009) 3187–3192.
[66] A. Rezanezhad, A. Hajalilou, F. Eslami, E. Parvini, E. Abouzari-Lotf, B. Aslibeiki, Superparamagnetic magnetite nanoparticles for cancer cells treatment via magnetic hyperthermia: effect of natural capping agent, particle size and concentration, J. Mater. Sci. Mater. Electron. 32 (19) (2021) 24026–24040.
[67] L.M. Kalossaka, A.A. Mohammed, G. Sena, L. Barter, C. Myant, 3D printing nanocomposite hydrogels with lattice vascular networks using stereolithography, J. Mater. Res. 36 (21) (2021) 4249–4261.
[68] S. Peng, Y. Li, L. Wu, J. Zhong, Z. Weng, L. Zheng, Z. Yang, J.-T. Miao, 3D printing mechanically robust and transparent polyurethane elastomers for stretchable electronic sensors, ACS Appl. Mater. Interfaces 12 (5) (2020) 6479–6488.
[69] G. Chen, X. Yang, X. Zhang, H. Hu, Water hydraulic soft actuators for underwater autonomous robotic systems, Appl. Ocean Res. 109 (2021), 102551.
[70] D. Liu, X. Liu, Z. Chen, Z. Zuo, X. Tang, Q. Huang, T. Arai, Magnetically driven soft continuum microrobot for intravascular operations in microscale, Cyborg and Bionic Syst. (2022), 9850832, 2022.
[71] G.R. Mahdavinia, S. Ettehadi, M. Amini, M. Sabzi, Synthesis and characterization of hydroxypropyl methylcellulose-g-poly(acrylamide)/LAPONITE® RD nanocomposites as novel magnetic- and pH-sensitive carriers for controlled drug release, RSC Adv. 5 (55) (2015) 44516–44523.